

www.acsanm.org Article

Rationally Designed Zwitterionic Peptides Improve siRNA Delivery of Cationic Diblock Copolymer-Based Nanoparticle Drug-Delivery Systems

Clyde Overby, Baixue Xiao, Tiana Salomon, Jorge Jimenez, Nathaniel Silvia, and Danielle S. W. Benoit*



Cite This: ACS Appl. Nano Mater. 2024, 7, 15193-15206



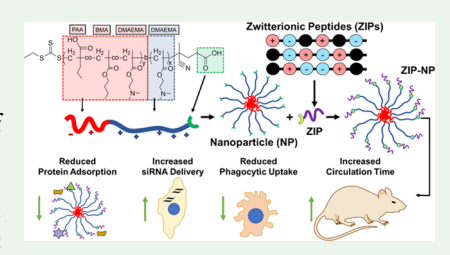
ACCESS I

Metrics & More

Article Recommendations

Supporting Information

ABSTRACT: Nanoparticle drug-delivery systems (NP DDS) have proven to be tremendously impactful for delivering therapeutic agents in cancer treatments, vaccinations, gene therapy, and diagnostics, and enabled agents such as RNA therapeutics. However, the exposure of NP DDS to biological milieus leads to the rapid adsorption of proteins and other molecules, forming a proteinaceous corona that obscures NP surface characteristics and controls the biological interactions of the NP DDS. Surface modifications, including poly(ethylene glycol) (PEG) and synthetic zwitterionic polymers, reduce protein adsorption yet lack monomer-scale tunability, have off-target immunological effects, and suffer from targeting-limited steric hindrance, altogether



motivating the development of alternative approaches. Peptides can uniquely form many zwitterions and have shown promise in reducing and controlling the NP protein corona as a function of the peptide sequence. However, the impact of zwitterionic peptides (ZIPs) on the drug-delivery properties of polymeric NPs has not been explored. In this work, diverse ZIPs computationally predicted to reduce protein adsorption by assessing peptide—peptide β -strand interaction energies were conjugated to pH-responsive cationic NPs. The resulting ZIP-NP conjugates exhibited up to 88% reduced protein adsorption and a range of siRNA-mediated gene knockdown that correlates with interaction energies. These data suggest that the peptide—peptide interaction energy is a promising design parameter for ZIPs for further model development. ZIP-NP also exhibited sequence-dependent variations in cellular uptake and circulation half-life, indicating that ZIP-NPs are suitable for tuning and improving NP drug-delivery characteristics.

KEYWORDS: nanoparticle drug delivery, zwitterionic peptides, siRNA delivery, peptide conjugates, antifouling

INTRODUCTION

Despite its instability and poor transport across cell membranes, RNA has proven to be an extremely versatile and powerful therapeutic through siRNA therapies, mRNA vaccines, and gene therapy through CRISPR/Cas9 mRNA delivery. Indeed, it is only through nanoparticle drug-delivery systems (NP DDS) that successful translation of the first siRNA therapeutic, Patisiran, and the mRNA SARS-CoV-2 vaccines was possible. NP DDS protects RNA and enables effective cellular uptake and cytosolic delivery in various applications, including local systemic delivery.

Beyond protecting against degradation and enabling intracellular delivery, NP DDS also improves the therapeutic efficacy of RNA by controlling biodistribution through targeting, incorporating environmentally responsive moieties, and altering pharmacokinetic profiles.^{2,6–9} siRNA delivery is enhanced using pH-responsive nanoparticle drug-delivery systems, which rely on micelles disassembling early endosomal vesicles and enabling endosomal escape.^{10,11} However, control over these properties in biological contexts has proven challenging due to protein adsorption and the formation of a protein corona.¹² The corona ultimately controls the biological interactions and behavior of NP DDS^{12,13} and can lead to aggregation, colloidal instability, reduced ligand targeting

efficacy, and increased mononuclear phagocytic system (MPS) uptake. 14–16 As serum proteins tend to be negatively charged, cationic RNA delivery systems are particularly prone to serum protein adsorption, which disrupts pH responsiveness and reduces cellular uptake and siRNA gene knockdown efficacy. 14

Designing NPs with antifouling properties, either inherently or through surface modifications, can mitigate protein adsorption. Still, only a few antifouling materials have been developed, with poly(ethylene glycol) (PEG) being the most widely used. PEGylation reduces protein adsorption and improves the circulation time of NP DDS up to 100-fold. However, improved pharmacokinetic half-life does not always manifest in improved tissue accumulation, suggesting a more complex relationship between PEGylated DDS pharmacokinetics and delivery efficacy. The balance between PEGylated DDS pharmacokinetics and delivery efficacy.

Received: April 4, 2024 Revised: June 14, 2024 Accepted: June 19, 2024 Published: June 27, 2024





tion-mediated increases in the circulation time of NPs with simultaneous reductions in tissue targeting and cellular uptake is sometimes referred to as the "PEG Dilemma", ²⁰ and recent investigations have suggested that the protein corona formed on PEGylated NP DDS is responsible for these behaviors.^{21–23} While PEG molecular weight,²⁴ polymer branching,²⁵ and surface functionalization density²⁶ have been investigated and found to alter NP protein corona, PEG has limited capacity for facile functional group additions (e.g., amines, carboxylates, etc.),23 which are highly impactful for the adsorption and maturation of the protein corona.²⁷ Additionally, PEG has been implicated in immunological reactions, which result in accelerated blood clearance (ABC) upon repeated administration, ^{28,29} and, in some cases, anaphylaxis. ^{30–32} Zwitterionic polymers ^{33,34} also reduce protein adsorption, increase the circulation time of NP DDS, and have been found to resist ABC with multiple systemic administrations.³⁵ Zwitterionic functionalities can imbibe similar antifouling properties at lower molecular weights and are, therefore, less disruptive to NP properties than PEG. 34,36-40 However, only a limited repertoire of biocompatible zwitterionic compositions exists, which may lead to similarly limited design space and, therefore, immunological concerns as PEG.

Zwitterionic peptides (ZIPs) offer a uniquely tunable alternative to PEG and other antifouling functionalities. 41 Peptide synthesis is highly controllable down to the monomer scale and commercially and synthetically mature, which allows the production of an exceptional variety of peptides with precise control over molecular structures. This level of specificity in structure allows for control over peptide—peptide and peptide-protein interactions, similar to how these sequence-specific interactions modulate protein-protein interactions. 42,43 Zwitterionic peptides also allow for a large design space; if only arginine, lysine, aspartic acid, and glutamic acid are considered, then more than 109 unique 15-mer peptides can be synthesized, with every additional amino acid increasing this number exponentially. This diversity may also provide a means to circumvent immunogenicity by substituting amino acids or ZIP sequences to design antigenically distinct peptides with similar antifouling or peptide-protein interactions and the observed resistance to ABC effects of zwitterionic polymers.³⁵

ZIP conjugation to gold nanoparticles (AuNP) reduced protein adsorption and enhanced the colloidal stability of AuNP in serum. 41 ZIP-AuNP protein corona development after serum exposure was correlated with the ZIP sequence and charge patterns rather than composition. The resulting different coronas lead to a dramatic alteration in phagocytic uptake in macrophages despite similar quantities of protein adsorption, representing a decoupling of cellular interactions from bulk protein adsorption. 41 While beneficial as a wellstudied and highly controllable model nanoparticle, AuNPs have limited uses in drug delivery. Therefore, here, we leverage ZIPs to modify a NP with long-standing use in drug delivery^{4,5,10,11,44–48} to investigate the effects of ZIP conjugation in a well-understood but relevant NP DDS. To explore the interactions of micellar NPs with ZIPs, a range of zwitterionic peptides with variable sequences were conjugated to cationic NP DDS for siRNA delivery. ZIP-NPs were evaluated for serum protein adsorption, stability, cellular uptake in mesenchymal stem cells (MSCs) and phagocytic macrophages, and cytotoxicity to MSCs and endothelial cells. ZIP-NPs were then evaluated for siRNA delivery efficacy,

protein-adsorption-mediated changes in pH-responsive endosomolytic behavior, siRNA complexation stability through heparin displacement and gel electrophoresis, and pharmacokinetics using an intravital infrared microscopy technique. Results indicate that ZIP conjugation to NPs decreases serum protein adsorption as a function of the predicted interaction energy, maintains siRNA-mediated gene knockdown in MSCs in serum, reduces macrophage uptake, and enhances systemic circulation time compared with unconjugated NP.

■ RESULTS AND DISCUSSION

Modulating protein adsorption is critical to NP DDS success due to the rapid formation of a protein corona in vitro and in vivo. Therefore, modifying NP surfaces with antifouling or "stealth" functionalities is vital for many applications but can disrupt NP structure and function. To understand the potential antifouling properties of zwitterionic peptides (ZIPs), ZIPs were synthesized using solid-phase peptide synthesis with the sequences with the predicted self-interaction energies (see Materials and Methods) listed in Table 1. Matrix-assisted laser

Table 1. Zwitterionic Peptides Synthesized and Used in This Work a

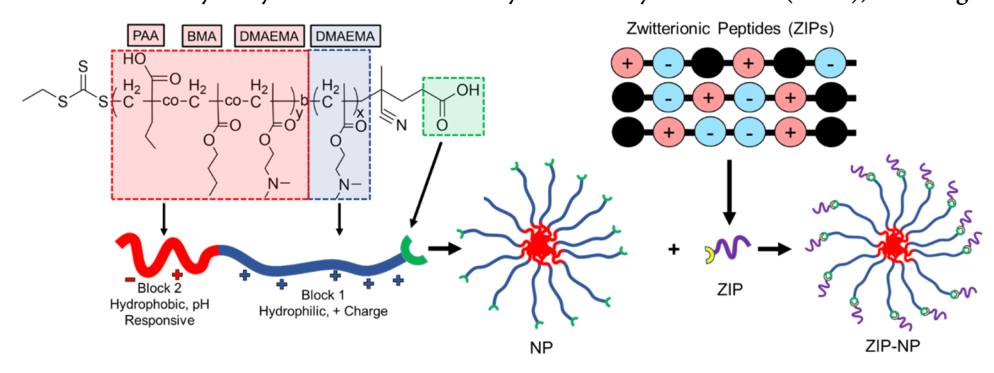
peptide number	peptide sequence	net charge	predicted self-assembly energy (kcal/mol)
1	SEESKEEKESKESKKG	-1	-2.42
2	EEEEEKSEKKKKSSSG	0	-2.9
3	KSSKEEKEKEEEKSKG	0	-0.85
4	KKKESEEKEESEKKSG	0	-0.36
5	KSKEEKSKEEKSKEEG	0	-0.05
6	KEKEKEKEKEKEKG	0	-4.72

"Peptides were synthesized using lysine, glutamic acid, and serine. ZIPs 1-5 were developed to have near-net-zero charge (± 1) and variable predicted self-interaction energies. ZIP6, a simple repeating sequence, was included for comparison. Net charge considers peptide N- and C-terminal groups and the loss of one amine group after conjugation.

desorption/ionization time-of-flight (MALDI-ToF) mass spectroscopy spectra for ZIPs are provided in Figure S2. ZIPs were then introduced to cationic pH-responsive diblock tercopolymer NP, previously demonstrated to be highly effective for in vitro 10,11,45 and local in vivo siRNA delivery 44,49 but prone to serum-mediated aggregation and inhibition of siRNA knockdown. 14 NP were comprised of 2-(dimethylamino)ethyl methacrylate (DMAEMA), butyl methacrylate (BMA), and propylacrylic acid (PAA) to form poly(DMAEMA)-b-poly-(DMAEMA-co-BMA-co-PAA). The polymer used in this study was analyzed by static light scattering size-exclusion chromatography to have a DMAEMA block 1 of 19 kDa and DMAEMA-co-BMA-co-PAA block 2 of 12 kDa, resulting in an overall molecular weight of 31 kDa and polydispersity index (PDI) of 1.08. ¹H NMR indicated a block 2 composition of 61% BMA, 21% DMAEMA, and 18% PAA (Figure S1). Using carbodiimide chemistry, ZIPs and amine-functionalized 2 kDa poly(ethylene glycol) were conjugated to NP at a 1:1 molar feed ratio, and the ZIP conjugation efficiency was measured via the amine-reactive o-phthaldialdehyde (OPA) assay (Figure S3). A graphical summary of the diblock synthesis and peptide conjugation to produce ZIP-NPs is provided in Scheme 1.

Physicochemical characteristics of ZIP-functionalized NP were analyzed. Transmission electron microscopy images

Scheme 1. Diblock Copolymers Composed of Dimethylamino Ethyl Methacrylate (DMAEMA), Butyl Methacrylate (BMA), Propylacrylic Acid (PAA), and Zwitterionic Peptides (ZIPs) Were Synthesized and Conjugated by N,N-Diisopropylcarbodiimide and N-Hydroxysuccinimide Chemistry in Dimethylformamide (DMF), Forming ZIP-NPs



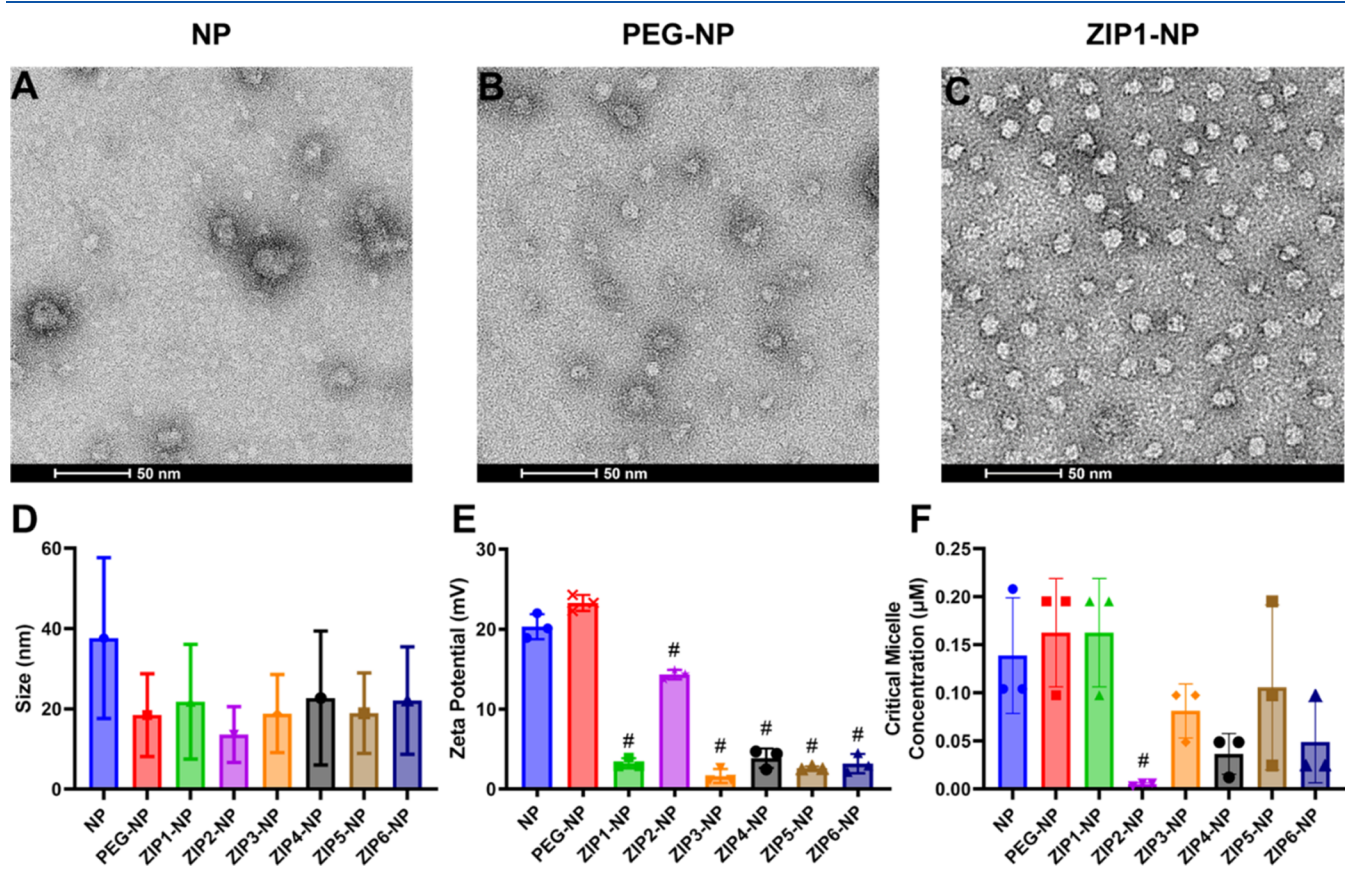


Figure 1. ZIP conjugation results in smaller, colloidally stable ZIP-NP conjugates. Transmission electron micrographs of (A) NP, (B) PEG-NP, and (C) ZIP1-NP indicate conjugation produces spherical micelles. (D) *Z*-average size of NP and NP conjugates in PBS indicates colloidal stability in physiological salt concentrations and a trend of decreased size after functionalization. Error bars are standard deviations calculated from PDI. (E) NP ζ potential is reduced by ZIP conjugation, while PEG conjugation does not statistically affect the ζ potential. (F) NP critical micelle concentration (CMC) is significantly decreased by ZIP2 conjugation, with other ZIPs and PEG not significantly affecting CMC. # indicates p < 0.05 when compared to NP using one-way analysis of variance (ANOVA) with Dunnett's post hoc.

indicate that NP, PEG-NP, and ZIP1-NP form spherical micelles (Figure 1A–C), suggesting functionalization does not disrupt NP shape or stability as measured in phosphate-buffered saline (PBS) (Figure 1D). However, all functionalized NPs were reduced in size compared to NPs as measured by dynamic light scattering (DLS) (Figure 1D). As micelle shape and size are controlled by the molecular weights and geometries of the hydrophobic and hydrophilic portions, on increased bulk in the hydrophilic region favors fewer polymers per nanoparticle and thus smaller nanoparticles, which is observed with both PEG and ZIP conjugation here. ζ potential

was also reduced by ZIP conjugation (Figure 1E) as expected due to the conjugation of net-neutral molecules. Despite the reduction in ζ potential, NPs remain stable in solution as expected due to the zwitterionic behavior. The had a greater ζ potential than other ZIPs, suggesting that the charges are not evenly distributed after conjugation, possibly due to the extended regions of positive and negative charges in the ZIP2 sequence. A summary of size, polydispersity, and ζ potential is provided in Table 2. Critical micelle concentrations (CMCs) were not statistically different between PEG and ZIP conjugates and NP except for ZIP2-NP, which had a greatly

Table 2. Summary of NP Conjugate Size (Z-Average) and ζ Potential^a

NP conjugate	diameter (nm)	ζ potential (mV)
NP	38 ± 20	20.3 ± 1.6
PEG-NP	20 ± 12	23.3 ± 1.0
ZIP1-NP	22 ± 12	3.2 ± 0.6
ZIP2-NP	12 ± 6	14.3 ± 0.6
ZIP3-NP	20 ± 11	1.6 ± 0.9
ZIP4-NP	22 ± 16	3.9 ± 1.2
ZIP5-NP	19 ± 10	2.6 ± 0.2
ZIP6-NP	22 ± 14	3.2 ± 1.2

^aError range is the standard deviation. Conjugation of NP with PEG or ZIPs decreases the NP size and maintains or increases polydispersity. ζ potential is reduced by conjugation with ZIPs.

reduced CMC (Figure 1F). The micelle-based NPs used here are in a thermodynamic equilibrium between an assembled NP state and a free solute state, and the contribution of self-assembling molecules on the surface may shift this equilibrium toward micelle formation, which would result in an altered CMC. The reduction in CMC observed with ZIP2-NP was expected due to the large negative (favorable) interaction energy. However, ZIP6-NP shows no change in the CMC despite having a similarly large negative interaction energy to ZIP2. As additional attractive forces in the micelle should lead to decreased CMC, the variable changes in CMC observed concerning the predicted interaction energy suggest that factors other than β -strand peptide—peptide interactions play a role in ZIP contributions to NP self-assembly, potentially including surface configuration and alignment.

The modeled expectations of ZIP-NP behavior are based on uniform ZIP conjugation to NP, as this is the configuration with the fewest assumptions. ZIP2, unlike other ZIPs, has highly uneven charge distribution with up to five consecutive negative and positive charges. As the conjugation reaction occurs via primary amines in the ZIPs, the biased distribution of lysine residues in ZIP2 likely contributes to a nonrandom orientation of ZIP2 in the NP corona. ζ potential analysis suggests that the positively charged region of ZIP2 is presented at the surface of ZIP2-NP due to its much higher potential than the other ZIP-NPs, suggesting that the negatively charged

region of ZIP2 is less accessible to the surface (Figure 1E). Electrostatic interactions between the positively charged DMAEMA polymer corona and the negatively charged region of ZIP2 may also be responsible for the difference in the ζ potential observed. Notably, all other ZIP designs contain no more than two consecutive charges of the same type and have much lower ζ potential than unconjugated NP and ZIP2-NP despite having similar compositions, indicating that these effects depend on the ZIP sequence and not bulk composition. PEG can adopt multiple configurations when conjugated to NP surfaces, including the looping "mushroom" conformation and the denser "brush" conformation, which greatly influence biological behaviors. ^{17,18} However, controlling linear PEG conformation on NP surfaces is limited to varying the conjugation density and PEG length. Therefore, sequencebased peptide-peptide or peptide-NP interactions drive the differences observed for ZIP-NP size and stability and may be used to influence surface conformation independently of composition.

To evaluate the antifouling behavior of ZIPs, ZIP-NPs were incubated with serum, and the resulting adsorbed protein was quantified. All ZIPs reduce the abundance of protein adsorbed onto the NP surface, with ZIP1-NP having adsorption similar to that of PEG-NP that is reduced by 88% vs unmodified NP serum protein adsorption. ZIPs reduced protein adsorption to NPs by 50-88% with an average of 68% reduction (Figure 2A). In the presence of serum, NP formed large aggregates immediately, visible as sedimentation and cloudiness, as reported previously, ¹⁴ indicating instability in serum. Under the same conditions, ZIP-NPs and PEG-NP solutions with serum remained clear and sediment-free, suggesting colloidal stability. Protein adsorption negatively correlates with the ZIP interaction energy (Table 1), as hypothesized, although the correlation is poor, indicating that β -strand interactions do not model the protein adsorption process completely in NP-ZIPs (Figure 2B). However, no relationship exists between ZIPprotein adsorption and the predicted β -strand interaction energy between ZIPs and the 50 most abundant serum proteins (Figure S4). Previous work has correlated ZIP sequence with specific serum protein affinity on ZIP-AuNP. 41 Therefore, more sophisticated ZIP models considering protein interactions beyond β -strand interactions, such as

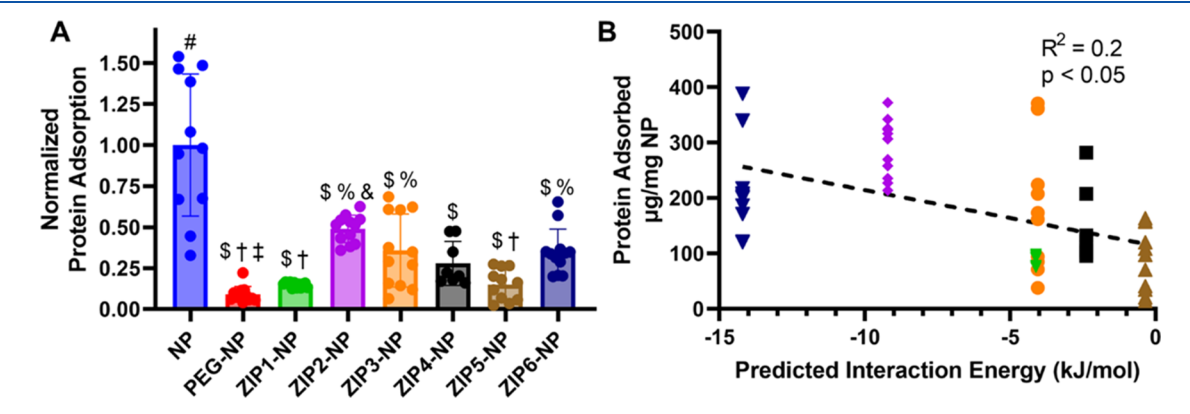


Figure 2. ZIP conjugation to NP reduces serum protein adsorption as a function of sequence and self-interaction energy. (A) ZIP functionalization greatly reduces protein adsorption, similar to PEG-NP in the case of ZIP1-NP. (B) β -strand self-interaction energy of ZIPs (Table 1) significantly but weakly correlates with the adsorbed serum protein. Note that neither PEG nor NP can be analyzed using peptide β -strand interactions and are absent as the β -strand interaction model only works between peptides. # indicates p < 0.05 vs all other samples, \$ indicates p < 0.05 vs NP, % indicates p < 0.05 vs PEG-NP, and indicates p < 0.05 vs ZIP1-NP, † indicates p < 0.05 vs ZIP2-NP, and ‡ indicates p < 0.05 vs ZIP3-NP via one-way ANOVA with Tukey's post hoc testing. Error bars indicate standard deviation.

electrostatic interactions, shape interactions, or intermediate protein—protein interactions in the growing corona, ¹² may enhance the predictive accuracy. Other interactions likely contribute to the variability in protein adsorption to ZIP-NPs.

While nanoparticle drug-delivery systems improve the safety profiles of chemotherapeutics⁵¹ and are safer than viral gene delivery vectors, 52 the necessary cationic components for oligonucleotide loading and endosomal escape also increase NP cytotoxicity. 6 Cationic nanoparticle toxicity is affected by the NP size, protein adsorption, cellular uptake, surface functionality, and composition, 14,45,46,53–55 which can be dose-limiting.⁵⁶ PEGylation has been found to reduce cationic NP cytotoxicity in macrophages, though this reduction is at least partially due to reduced cellular uptake. 57 To investigate the effects of ZIP conjugation on NP cytotoxicity, a murine mesenchymal stem cell line (C3H10T1/2), representing potential cellular target, was treated with 30 nM GAPDH siRNA loaded into NPs with a 4:1 NP/siRNA charge ratio, which represents a siRNA dose previously found to be highly effective in silencing these cells. ¹⁴ In the presence of serum, all NP and NP conjugates are cytocompatible over 24 h (Figure S5A), corroborating previous gold NP-ZIP conjugate investigations. 41 In serum-free conditions, NP treatments reduce cell viability to 15%. In contrast, cells treated with the ZIP-NP conjugates exhibited >70% viability, suggesting cytocompatibility is significantly improved through ZIP conjugation (Figure S5B). In the presence of serum, 30 nM siRNA-loaded NPs, PEG-NPs, and ZIP-NPs do not exhibit cytotoxicity over 24 h in human umbilical vein endothelial cells (HUVECs), which were used as an analogue for blood vessel endothelial cells that would be exposed upon systemic administration (Figure S6). The mechanism of cationic polymer and NP toxicity is typically attributed to interactions with mitochondrial membranes,⁵⁸ and the absence of toxicity in ZIP-NPs compared to NP could be due to alterations in mitochondrial interactions or reduced cellular uptake and delivery efficacy, thus limiting mitochondrial exposure to NP. Hence, delivery efficacy was further explored.

siRNA-mediated gene knockdown using cationic, pHresponsive NPs is greatly inhibited by serum protein adsorption.14 As ZIPs reduce protein adsorption and aggregation, siRNA delivery efficiency should be improved compared to that of unfunctionalized NP. Therefore, GAPDH siRNA delivery efficacy was investigated using C3H10T1/2 cells, a murine mesenchymal stem cell line (Figure 3). Compared to nontargeting siRNA-loaded NP controls, GAPDH siRNA-loaded NP reduced relative GAPDH expression by 65%, while PEG-NP reduced expression by 85% (Figure 3A). ZIP-NP had variable GAPDH knockdown efficacy, ranging from ~75% (ZIP1-NP and ZIP2-NP) to no significant knockdown (ZIP4-NP, ZIP5-NP, and ZIP6-NP). siRNA knockdown efficacy correlates with the predicted ZIP self-interaction energy for ZIPs 1–5 but not ZIP6 (Figure 3B), suggesting that ZIP-NP corona specificity or stability also impacts delivery efficiency. This is particularly evident with ZIP2-NP, which has high protein adsorption, reduced CMC vs unfunctionalized NP, high predicted β -strand interaction energy, and siRNA knockdown similar to those of ZIP1-NP and PEG-NP. In contrast, ZIP5 has the highest predicted β strand interaction energy (unfavorable) and no statistically significant siRNA knockdown. Without serum, all NP and NP conjugates reduce GAPDH expression by over 75% (Figure 3C). Comparing serum vs no-serum conditions indicates

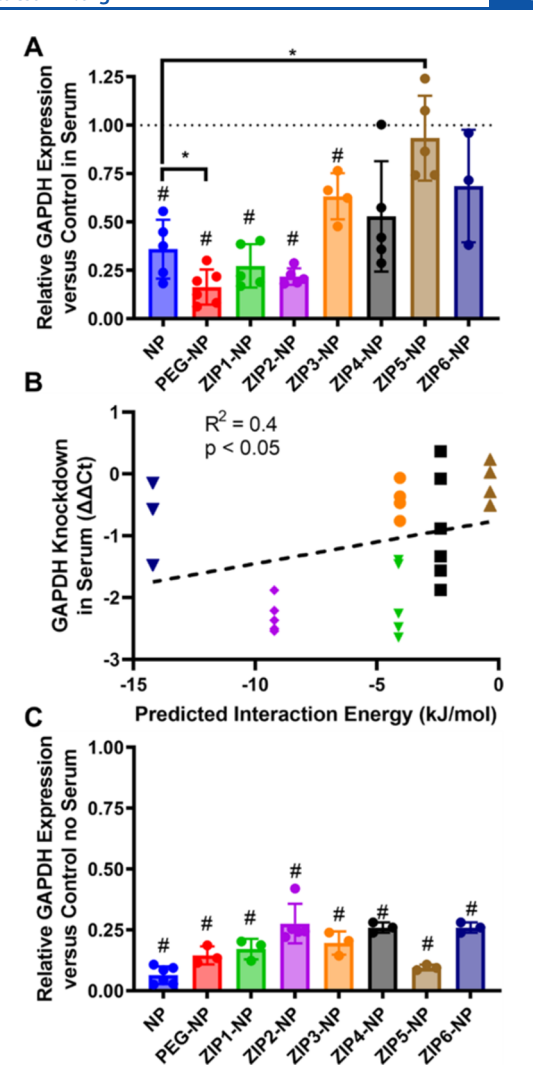


Figure 3. ZIP-NP maintains or inhibits siRNA-mediated gene knockdown in a sequence-dependent manner compared to NP and reduces NP cytotoxicity in the absence of serum after 24 h of treatment. (A) GAPDH knockdown through 30 nM siRNA delivery by ZIP-NP varies by ZIP sequence. ZIP1, ZIP2, and ZIP3 significantly reduce GAPDH knockdown compared to negative siRNA-loaded NP controls, while ZIP4, ZIP5, and ZIP6 do not. While ZIP1-NP and ZIP2-NP trend toward lower GAPDH expression than NP, only PEG-NP has significantly reduced GAPDH expression compared to NP. GAPDH expression normalized to β -actin expression. (B) Knockdown efficacy correlates with decreasing ZIP interaction energy. (C) Without serum, all NP conjugates significantly reduce GAPDH expression vs negative controls. All GAPDH expression normalized to negative control siRNA-loaded NP-treated cells. * indicates p < 0.05between samples, # indicates p < 0.05 vs controls via one-way ANOVA with Tukey's post hoc testing (A, C).

serum inhibits siRNA delivery as previously described, ¹⁴ likely due to the effects of protein adsorption and aggregation. The reduced siRNA knockdown difference of ZIP and PEG-functionalized NPs between serum and no-serum conditions suggests that these NP conjugates are less sensitive to protein adsorption than NP, suggesting they are effective antifouling modifications for improving siRNA delivery.

Altered siRNA-mediated gene knockdown by ZIP functionalization may be due to alterations in one of many steps in the delivery sequelae: siRNA complexation and protection, cellular uptake, and endosomal escape. As a first step in investigating

the mechanisms underlying changes in siRNA delivery efficacy, cellular uptake was measured by flow cytometry after treatment with fluorescently labeled siRNA-loaded NPs. After 24 h of treatment in either serum-containing or serum-free conditions, more than 95% of MSCs were positive for siRNA. In serum, only ZIP1- and PEG-NP conjugates increased intracellular siRNA uptake relative to NP, while ZIP2 and ZIP4 significantly reduced uptake (Figure 4A). Linear regression

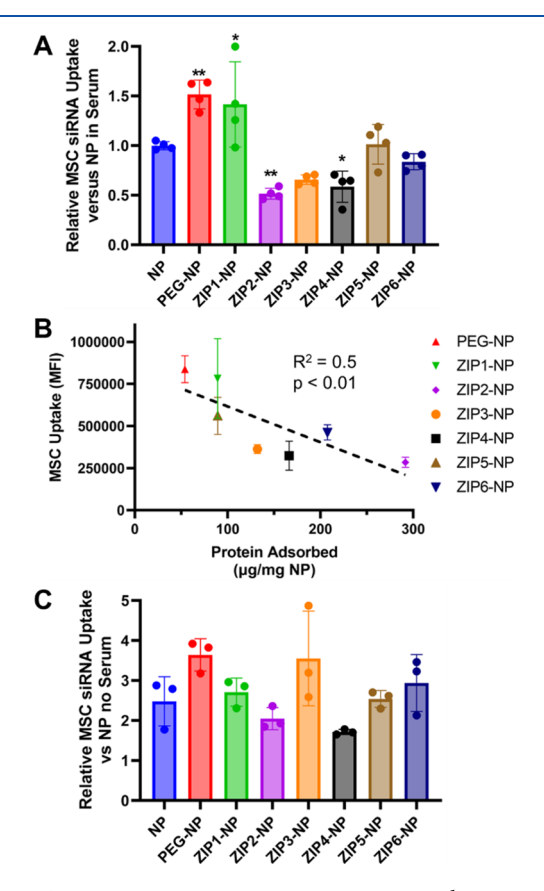


Figure 4. ZIP1 conjugation increases siRNA accumulation in MSCs relative to NP only in the presence of serum as a function of protein adsorption. (A) After 24 h of incubation, relative siRNA uptake in MSC is increased for ZIP1 and PEG conjugation, while ZIP2- and ZIP4 significantly reduce siRNA uptake in the presence of serum. (B) Linear regression of MSC uptake vs protein adsorption among ZIP conjugates reveals MSC uptake is inversely correlated with protein adsorption. (C) In the absence of serum, no significant differences in siRNA uptake are observed in any ZIP-NP compared to NP. Values normalized to NP uptake in serum. Note: mean NP siRNA uptake was 2.5-fold higher in the absence of serum compared to that in the presence of serum. More than 95% of all MSCs contained labeled siRNA after 24 h incubation. * indicates p < 0.05, ** indicates p < 0.01 using one-way ANOVA with Dunnet's post hoc testing.

analysis between protein adsorption and siRNA uptake in MSC among NP conjugates reveals a strong inverse correlation between uptake and protein adsorption (Figure 4B), suggesting that higher serum protein adsorption results in low uptake of ZIP2 and ZIP4 conjugates compared to other NP conjugates. This correlation does not hold for unconjugated NP, which suggests a limit to this observed relationship that may be caused by protein corona identity or other effects. While not all of the MSC uptake variation of the NP conjugates is attributable to protein adsorption, no correlation was observed between ZIP β -strand interactions and uptake in

serum. In the absence of serum, all ZIP conjugates had statistically equivalent uptake relative to NP, although ZIP3-NP had a trend toward higher uptake (Figure 4C). However, the mean fluorescence intensity of all NP-treated MSCs without serum was 2.5-fold higher than that for cells treated in the presence of serum, indicating that serum inhibited intracellular uptake of NP and NP conjugates.

While MSC uptake and protein adsorption correlate, the variation in ZIP-NP MSC intracellular uptake does not explain the siRNA knockdown efficacy observed in Figure 3. Therefore, changes in pH-responsive endosomal escape due to ZIP functionalization were investigated. NPs were tested for hemolytic activity, which measures the ability of pH-responsive NPs to disrupt red blood cell membranes at various pH. Hemolysis revealed a trend of increasing membrane disruption with ZIP and PEG functionalization compared to NP, except for ZIP2-NP in the absence of serum (Figure 5A). Membrane

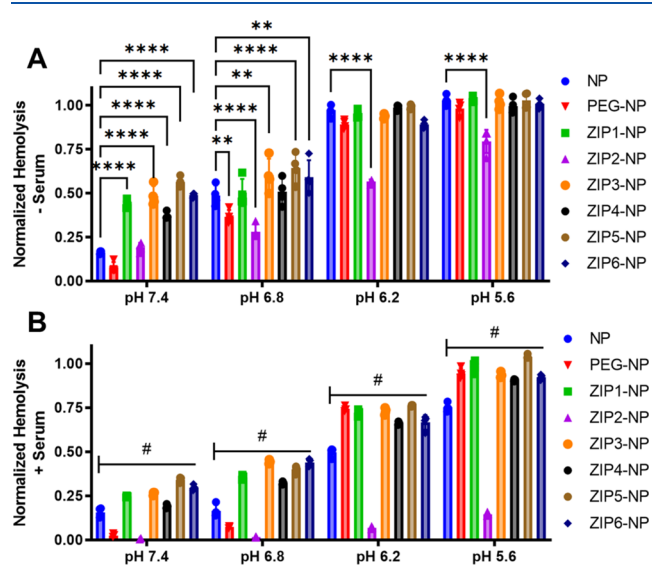


Figure 5. NP pH-responsive membrane disruption is increased by ZIP functionalization. (A) Hemolysis assay results in the absence of serum. Except for ZIP2-NP, at pH 6.2 and 5.6, all functionalized NPs are similar to NP with nearly 100% hemolysis, suggesting that ZIP functionalization does not interfere with pH-responsive membrane disruption in endosomal conditions. Except for ZIP2 and ZIP4, ZIP functionalization increases hemolysis at pH 7.4 and 6.8. At endosomal pH, ZIPs (except ZIP2) perform similarly to PEG-NP. (B) Hemolysis assay results in the presence of 10% human serum. Except for ZIP2, all ZIPs exhibit increased hemolytic activity at all pH values tested over NP, suggesting that ZIP functionalization inhibits serum-induced aggregation similarly to PEG. *p < 0.05, **p < 0.01, ****p < 0.001 by one-way ANOVA with Tukey's post hoc testing, p = 4

disruption at neutral pH is typically associated with cytotoxicity, ⁵⁹ which is only observed with unfunctionalized NP without serum (Figure S5B). In serum conditions, NP lost hemolytic activity compared to no-serum conditions at all pH values and had significantly reduced hemolytic capacity at endosomal pHs compared to all NP conjugates except ZIP2-NP, which had less than 20% hemolysis in all serum-containing conditions (Figure 5B). As previous investigations have found, serum-induced aggregation can inhibit pH responsiveness and endosomal escape, suggesting that serum-adsorbed ZIP2-NP is more thermodynamically stable against disassembly than other ZIP-NPs. All other ZIP-NP conjugates had higher hemolytic

activity than NP in serum. Together, these results show that reduced protein adsorption mediated by ZIPs maintains pH-responsive membrane destabilization of NPs.

Previous reports have found that siRNA release from NP, which is necessary for integration into knockdown machinery intracellularly, is hindered by serum protein adsorption to NPs. To evaluate the impact of ZIP functionalization on siRNA release, a heparin competition assay was used. siRNA-loaded ZIPs were incubated in 10% human serum overnight before incubation with a range of heparin concentrations for 30 min. Heparin, a polyanion, competes electrostatically with siRNA, resulting in the release from NP. Samples were then separated by electrophoresis at pH 7.4 using agarose gels, and after staining, the fluorescence intensity was normalized to free siRNA for each heparin concentration (Figure 6A). At 0.32

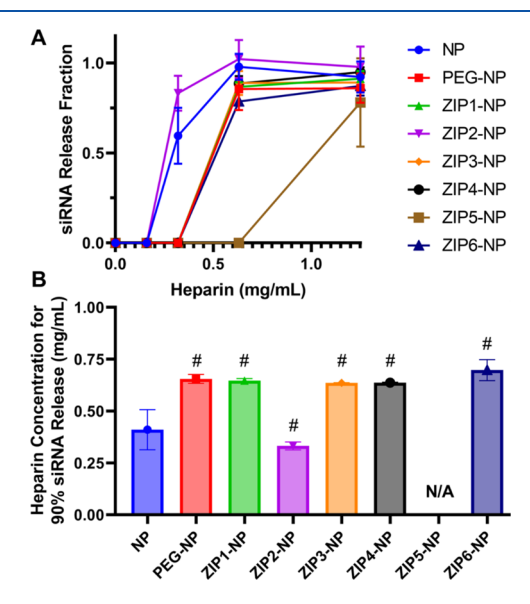


Figure 6. siRNA release from serum-incubated NPs is reduced by ZIPs except for ZIP2. (A) Profile of siRNA release normalized to free siRNA at increasing sodium heparin concentrations. As heparin concentration increases, it electrostatically competes with siRNA to cause release, which is then measured by electrophoretic separation and fluorescence staining. NP and ZIP2-NP have significantly higher siRNA release at 0.32 mg/mL heparin than all other conjugates. (B) Calculated heparin concentration for 90% siRNA release derived from sigmoidal curve fitting using GraphPad Prism. Lower values indicate a lower concentration of heparin needed to displace 90% of loaded siRNA. ZIP5-NP's 90% release concentration could not be calculated due to instabilities in fitting the data, but ZIP5-NP had the lowest siRNA release of any conjugate at 0.63 and 1.25 mg/mL heparin. # indicates p < 0.05 vs NP based on 95% confidence interval from nonlinear fitting, n = 3 for each condition and sample. Error bars indicate standard deviation.

mg/mL, ZIP2-NP had improved siRNA release compared to NP and all other NP conjugates, despite having the lowest observed hemolytic potential in serum, which may explain the high siRNA knockdown efficacy of ZIP2-NP in serum. At 0.63 mg/mL heparin, most conjugates were similar to NP except for ZIP5-NP and ZIP6-NP, which had lower siRNA release than NP. Curve fitting was applied to the siRNA release profiles to derive an equation to calculate the estimated concentration of heparin to release 90% of the loaded siRNA for each NP (Figure 6B). Except for ZIP2-NP, ZIP conjugation increased the concentration of heparin required to displace siRNA, indicating that ZIP conjugation increases the stability of

electrostatic binding of siRNA except for ZIP2-NP. ZIP2-NP's behavior may result from the previously discussed heterogeneities in peptide conjugation due to the nonuniform electrostatic charges of ZIP2, which may lead to more surfacelocalized siRNA than other ZIP-NPs. ZIP5-NP's observed response was unsuitable for this curve fitting analysis due to only releasing detectable siRNA at 1.25 mg/mL heparin concentration. ZIP5-NP has the lowest predicted selfinteraction potential and among the lowest protein adsorption of all ZIP conjugates but has a poor siRNA knockdown efficacy likely explained by this observed poor siRNA release. Changes to the protein corona caused by ZIP or PEG conjugation may impact heparin accessibility to the cationic poly(DMAEMA), thus inhibiting heparin competition. 14 These data challenge the idea that protein adsorption inhibits endolysosomal escape emulated here via hemolysis, which fails to correlate with either protein adsorption or siRNA release and again demonstrates the varied impact of ZIP sequence on individual aspects of NP drug-delivery properties.

Successful systemic NP delivery requires that the NPs are available for uptake by the target cell type and have a sufficient circulation time to achieve the desired target dose. While delivery of siRNA-NPs to therapeutic targets such as MSCs in vitro is relevant to mechanisms of therapeutic action, the in vivo delivery of NP DDS involves NP interaction with myriad off-target cell types, and particularly phagocytic cells that compete for NP uptake and clearance in both local and systemic delivery. 60 Phagocytic cells in the MPS strongly influence pharmacokinetic properties of NP in systemic delivery. 60,61 Phagocytic uptake of NP DDS is driven by scavenger receptors, potentiated by opsonins or denatured proteins adsorbed to the NP surface, 21 suggesting that reduction in protein adsorption on NP by surface modification may reduce phagocytic uptake. To investigate the impact of ZIP functionalization on macrophage NP uptake, RAW 264.7 murine macrophages were treated with ZIP-NP complexed with siRNA in the presence of serum. At 2 h, all conjugates except ZIP6-NP had reduced macrophage uptake compared to unfunctionalized NP, with ZIP-NPs 1, 2, and 5 having similar uptake to PEG-NP (Figure S7A). Mean fluorescence intensity of NP+ cells was used to measure relative intracellular siRNA abundance, which was also reduced by ZIPs 1-5 and PEG (Figure S7B). The relative abundance of intracellular siRNA was similar between PEG-NP and ZIP-NPs 2, 4, and 5. As ZIP functionalization also increases nonphagocytic cellular uptake in the presence of serum, a different mechanism, such as endocytosis, instead of or together with phagocytosis may underlie the observed uptake in macrophages. In the absence of serum, nearly all macrophages are NP+ (Figure S7C), but the intracellular siRNA abundance is generally reduced by ZIP conjugation (Figure S7D). These results corroborate previous reports that antiphagocytic "stealth" behavior depends on protein adsorption. 61,62 The behavior of ZIP-NPs is similar to PEG-NPs in both the presence and absence of serum, indicating that ZIPs have similar antiphagocytic properties as PEG in addition to antifouling properties. Nevertheless, in vitro macrophage uptake is only a rough correlate for pharmacokinetics, motivating further investigating ZIP-NP behavior in vivo.

Circulation time is a critical parameter for NP DDS success and is controlled by NP size, physicochemical properties, and protein corona. ^{6,27,63,64} To evaluate changes in NP circulation time after ZIP modification, an in vivo infrared microscopy

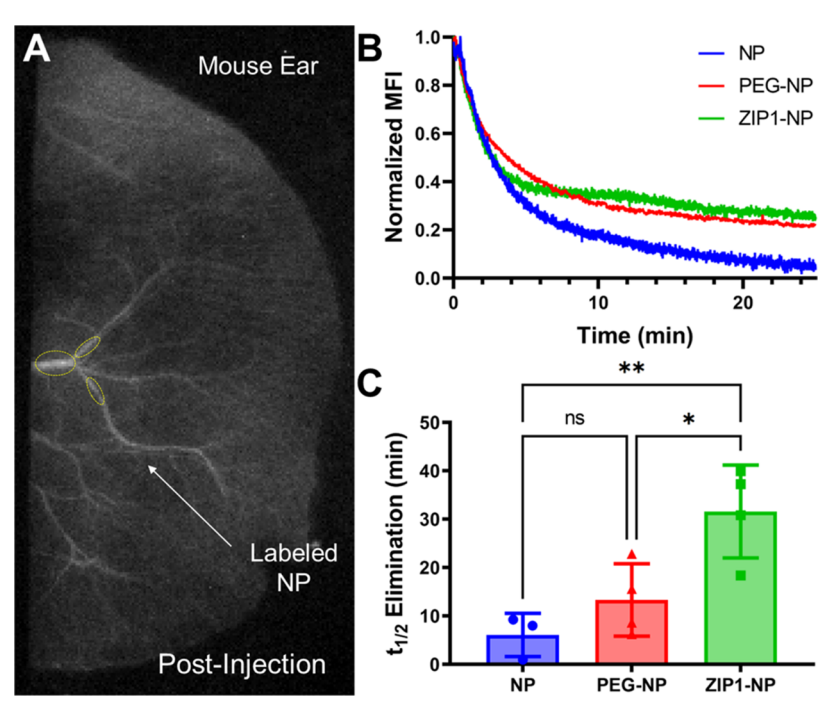


Figure 7. Pharmacokinetic half-life of NP is improved by ZIP1 conjugation. Infrared dye labeled NP, PEG-NP, and ZIP1-NP were administered retroorbitally to anesthetized mice at 4 mg/kg. (A) Infrared fluorescence microscopy was used to image the mouse ear over time. The fluorescence intensity in the ear was tracked in blood vessels, as shown by the regions of interest (ROI) (yellow ovals). (B) Background intensity of the ROIs before injection was subtracted from before combining ROI intensity and normalizing to peak intensity and background intensity. (C) Fitting a two-phase decay model to the data reveals the elimination half-life of ZIP1-NP to be nearly 5-fold increased over NP and more than 2-fold over PEG-NP. *p < 0.05, *p < 0.01. GraphPad Prism two-phase exponential decay model used for evaluation with plateau fixed to the preinjection ROI luminosity. One-way ANOVA used with Tukey's post hoc analysis used for statistical comparison. Error bars indicate standard deviation.

system was used to longitudinally track fluorescently labeled NP in blood vessels in the ears of mice after intravenous administration (Figure 7). The technique of tracking the intensity of fluorescently labeled micelles in mouse ear blood vessels has been demonstrated to provide accurate pharmacokinetic data with fewer mice. 36,65 ZIP1-NP was selected for this experiment due to its similarity, low observed protein adsorption and cytotoxicity, and high MSC siRNA delivery efficacy and having the most similar behavior to PEG. Cy7labeled NPs were injected retroorbitally into isofluraneanesthetized mice at a 4 mg/kg dose, approximating a 30 nM siRNA whole-body dose corresponding to significant siRNA knockdown measured in vitro, and fluorescence was recorded via an infrared camera (Figure 7A). The resulting pharmacokinetic profiles were fit against two-phase elimination models (Figure 7B), yielding distribution phase and elimination phase half-lives. ZIP1-NP greatly increased the elimination half-life to 32 min, a 5-fold increase over NP at 6 min, and a nearly 2.5-fold increase over PEG-NP, which had an elimination half-life of 13 min (Figure 7C). As ZIP1-NP and PEG-NP had similar size, protein adsorption, and stability, this suggests that changes in the protein corona are responsible for the increased circulation time of ZIP1-NP over PEG-NP.

The goal of this work was to investigate a new zwitterionic peptide-based paradigm as an antifouling modification for the cationic siRNA nanoparticle drug-delivery system. The underlying hypothesis is that the sequences of the zwitterionic peptides could be used to modulate ZIP-NP physicochemical properties and biological interactions by modeling peptide—peptide interactions. The results indicate that ZIPs are effective antifouling modifications for NPs by reducing protein adsorption, increasing siRNA uptake, reducing phagocytic

uptake, and improving systemic circulation time. Specific ZIP designs, particularly ZIP1, perform similarly to PEG-NP in these metrics in vitro and more than 2-fold higher circulation time in vivo. ZIPs demonstrated several unique qualities compared with PEG in these experiments, including decoupling of protein adsorption from cellular uptake and sequence-dependent but not composition-dependent changes in physicochemical properties and biological interactions.

ZIPs have several advantages over existing antifouling functionalities used to modify NPs. ZIPs exhibit sequencedependent behavior, as evidenced by the disparate behaviors of ZIPs 1 and 6, which have nearly identical bulk composition, and suggests that further developments of models of ZIP behaviors and interactions with proteins may allow for tunable behavior as a function of sequence. Existing materials, such as PEG and poly(carboxybetaines), have limited monomer-level tunability in comparison due to both synthesis conditions and the limited variety of suitable substitutable monomers. In comparison, ZIPs have tremendous diversity, enabling a large design space for tailoring ZIP properties to a particular application. For the cationic, pH-responsive NP used here, maintaining similar NP physicochemical properties while enhancing NP colloidal stability in the presence of serummaintained siRNA delivery capabilities and greatly increased circulation times. The thermodynamic contribution of the ZIPs was tunable and may allow for further control of the ZIP-NP system for pH responsiveness. Additionally, laboratory-scale peptide synthesis techniques are well-developed and allow for a large variety of ZIPs to be synthesized without the need for reaction optimization and new protocol development.

Computational modeling of ZIP interactions provides an avenue to predictive biomaterial design approaches for NP

conjugates. β -strand interactions predicted protein adsorption, siRNA knockdown efficacy, and macrophage uptake and provided a basis for initial ZIP design in siRNA delivery applications. Notably, β -strand ZIP-ZIP interactions are computationally efficient to calculate compared to more sophisticated peptide-protein interaction predictions, which are prohibitively computationally expensive to calculate as a primary in silico screening method for antifouling. However, these design principles are based on assumptions about the uniformity of peptide presentation on NP surfaces, which are unlikely to be completely accurate and cannot be verified with existing techniques for nanoparticle characterization. The complex physics of the NP surface, peptide, and protein interactions are not fully understood and necessitate further investigation to exploit these interactions to form favorable protein coronas and improve NP DDS. Fortunately, the recent development of machine learning approaches to protein folding and protein-protein interaction modeling⁶⁶ offers greater computational efficiency to accurately predict ZIPpeptide and ZIP-protein interactions. While limited data currently exist to train such models, the facile chemical synthesis of varied ZIPs and ZIP-NPs provides a pathway to quickly generate the data sets needed for training.

ZIP2-NP is an outlier for both serum-free and serumcontaining experiments. This is likely due to the design's long positive and negative charge segments and high self-interaction energy, which manifested in lower CMC than other ZIP conjugates (except for ZIP6) and correlates with the highest protein adsorption measured among ZIP-NPs. However, ZIP2-NP readily releases siRNA after protein adsorption in the presence of heparin and exhibits similar siRNA knockdown efficacy to ZIP1-NP and PEG-NP in serum despite poor pHresponsive membrane disruption and lower cellular uptake, indicating that other interactions likely explain ZIP2-NP's bioactivity. This unusual combination of properties may be due to selectivity in protein adsorption, leading to changes in endocytosis or cellular response or the orientation of ZIP2 conjugation to the polymer, as ZIP2 is amine-rich on the carboxy terminus rather than relatively even distribution as in other ZIP sequences. Indeed, the identity of proteins within the ZIP-NP corona may be controlled based on ZIP corona as previously observed in gold NPs, 41 offering additional means to impact delivery. Proteins in NP coronas are potent biodistribution and pharmacokinetic modifiers, 63 and control over NP corona composition is crucial for controlling the NP behavior in vivo for improving nanomedicine. 12,13,64 Current techniques for controlling protein coronas involve preincubation in purified proteins from serum, which is a complex and expensive strategy for potential therapeutic use. ZIPs offer the opportunity to control protein corona without preincubation through selective peptide-protein interactions in vivo, and ZIP composition is more finely controllable than other antifouling materials in part due to the step-by-step peptide synthesis process, making ZIPs both a highly flexible and precise foundation material for controlling NP protein corona.

CONCLUSIONS

Modifying NPs with antifouling materials is paramount to enabling their use in systemic administration, particularly for cationic NPs with a high propensity for aggregation in the presence of serum proteins. This work demonstrates that zwitterionic peptides can be designed to act as antifouling NP functionality while also maintaining NP drug-delivery efficacy,

enabled by the many diverse zwitterionic peptides attainable. Uniquely, the self-interaction potential of ZIPs correlated with protein adsorption, critical micelle concentration, and siRNA knockdown efficacy. Simultaneously, the large design space of zwitterionic peptides affords the ability to screen through related ZIPs for specific delivery outcomes that can be experimentally verified and may prove useful for generating sufficient data in the future to enable accurate ZIP design with reduced experimental burdens.

Further exploration of interactions between the ZIP sequence, protein corona identity, and drug-delivery behavior, such as pharmacokinetics and biodistribution, could provide greater insight into NP design and modification. The chemical tunability of ZIPs provides a greater flexibility for interrogating the mechanisms of NP surface interactions with proteins than existing modifications with less-controlled synthesis. Additionally, it may be possible to extend more accurate and computationally expensive protein—protein or peptide—peptide interaction models to ZIP-NPs. As machine learning models become more accurate and efficient, it may be possible to combine experimental approaches with guidance from these models to select behaviors, including protein adsorption, critical micelle concentration, circulation time, cell type specificity, or protein corona profile.

MATERIALS AND METHODS

Materials and Equipment. All materials, unless otherwise specified, were sourced from Sigma-Aldrich. Dynamic light scattering (DLS) was conducted by using a Malvern Zetasizer. Size-exclusion chromatography was conducted using a Tosoh Super HM-N chromatography column connected to a Wyatt Technologies Treos light scattering instrument and a Wyatt Technologies T-rEX differential refractometer. ¹H nuclear magnetic resonance measurements were performed on a Bruker Avance 400 or 500 MHz spectrometer and were performed in deuterated chloroform, unless otherwise noted. Matrix-assisted laser desorption-ionization mass spectrometry time-of-flight (MALDI-ToF) measurements were conducted using a Shimadzu Axima Confidence MALDI instrument. All cells were cultured at 37 °C in 5% CO₂.

Zwitterionic Peptide Design. Zwitterionic peptide (ZIP) design was accomplished through a nonbiased random assembly of zwitterionic peptides followed by screening for peptide-peptide β strand interactions using an algorithm adapted by Trovato et al.⁶⁷ and previously used by Overby et al. 41 Briefly, ZIPs were randomly assembled and then their β -strand interactions with themselves were calculated using the methods described by Trovato et al.⁶⁷ Within a net charge limit of ± 1 , amino acids lysine (positive), glutamic acid (negative), or serine (hydrophilic and neutrally charged) were assembled in silico into peptides. 5000 peptide sequences were generated at a time as zwitterionic peptides (ZIPs). Peptide sequences were then compared in parallel and antiparallel orientations with a sliding window of 6 or more amino acids with a per-residue entropic contribution of 0.2 kcal/mol using a python script adapted from methods described by Trovato et al. 67 to yield β -strand interaction energies. ZIPs were then ranked by the average interaction energy of their discrete peptides, with the highest (positive) interaction energy corresponding to the lowest propensity for self-assembly. A Github repository containing the Python script used to simulate peptidepeptide interactions can be found at the following link: https:// github.com/coverbyur/AFPepPro.

Peptide Synthesis and Characterization. Peptides were synthesized using automated, microwave-assisted solid-phase peptide synthesis (CEM Liberty1) via diisopropylcarbodiimide and OxymaPure coupling of Fmoc-protected amino acid precursors on Gly-Wang resin at 0.25 mmol scales. 10% Piperazine in 90/10% dimethylformamide (DMF)/ethanol was used for Fmoc deprotection. Semirandomized peptides were synthesized using stoichiometric

ratios of amino acid precursors representing proportionality to the desired incorporation probability. Peptides were cleaved in 92.5% trifluoroacetic acid, 2.5% water, 2.5% triisopropylsilane, and 2.5% 3,6-dioxa-1,8-octanedithiol for 2 h at room temperature before precipitation into 0 °C diethyl ether. After three diethyl ether wash and centrifugation cycles, peptides were dried under vacuum. Peptide molecular weights and molecular weight distributions were determined using matrix-assisted laser desorption-ionization time-of-flight mass spectroscopy (MALDI-ToF MS) (Shimadzu Axima Confidence) using α -cyano-4-hydroxycinnamic acid as matrix.

Nanoparticle Synthesis and Characterization. Cationic diblock copolymer was synthesized for this study using reversible addition-fragmentation chain transfer (RAFT) polymerization as previously described by Convertine and Benoit et al. 10 DMAEMA and BMA monomers were purified from inhibitors using vacuum distillation at approximately 130 °C and 200 Pa of absolute pressure. Propylacrylic acid was synthesized from diethyl propylmalonate in a method adapted from Jiang et al.⁶⁸ Briefly, 5 g of diethyl propylmalonate (24.7 mmol) was hydrolyzed in 40 mL of 2 M NaOH overnight at room temperature while stirring vigorously. Approximately 3 mL of 13 M HCl was added until the solution pH was 1 and then the mixture was extracted three times with 80 mL of ethyl acetate. The ethyl acetate was dried with MgSO₄ before rotary evaporation to yield colorless crystalline propylmalonate diacid (2.83 g, 20.1 mmol). The diacid was then dissolved in ice cold ethyl acetate to 0.75 M to which 905 mg of paraformaldehyde (30.2 mmol) and 1.48 g (20.3 mmol) of diethylamine were added in a stirred flask. The reaction was then allowed to warm to room temperature over 1 h before being refluxed overnight on a 80 °C oil bath. 12 mL of water was added, and then 13 M HCl was added until the pH was approximately 1. The mixture was then extracted using 3× 75 mL of ethyl acetate, combined and dried with MgSO₄. The crude propylacrylic acid was dried under vacuum to yield a colorless oil. The crude PAA was then purified via gel filtration chromatography using Geduran Si 60 stationary phase and 2:1 v/v pentane ether:ethyl acetate mobile phase. The PAA has an Rf of approximately 0.8 and so elutes quickly. 1.86 g (16.3 mmol) of purified PAA was recovered as a colorless thin oil (yield 66%) and analyzed with ¹H NMR (CDCl₃, 500 MHz): 0.92 (t, 3H), 1.51 (m, 2H), 2.26 (t, 2H), 5.63 (s, 1H), 6.28 (s, 1H). No impurities were detected by ¹H NMR.

Briefly, polymerization was conducted in two stages to form the two blocks. The first block was synthesized utilizing the chain transfer agent (2-cyano-5-(ethynylamino)-5-oxopentan-2-yl ethyl carbonotrithioate) (ECT) and 2,2'-azobis(2-methylpropionitrile) (AIBN) as a free radical initiator along with dimethylamino ethyl methacrylate (DMAEMA) in 40 wt % dimethylformamide (DMF). ECT was synthesized as described by Convertine and Benoit et al. 10 AIBN was recrystallized in methanol before synthesis. Reagents were combined with a 5:1 ECT/AIBN ratio with a target degree of polymerization of 150 for a theoretical molecular weight of 23.6 kDa. The reagents were combined and purged with nitrogen for 45 min before heating to 60 °C for 6 h. The polymer was then precipitated in ice cold 80/20% (v/ v) pentane/diethyl ether and dried in vacuum. The first block polymer was then analyzed via size-exclusion chromatography and static light scattering and found to have a molecular weight of 19 kDa with a PDI of 1.03. The second block was synthesized using 5:1 first block to AIBN molar ratio and 25% DMAEMA, 25% propylacrylic acid (PAA), and 50% butyl methacrylate (BMA) (molar basis) with a target degree of polymerization of 110 in 40 wt % DMF at 60 °C for 24 h. After precipitation in 80/20% (v/v) pentane/diethyl ether, the samples were dried in vacuum and analyzed with size-exclusion chromatography, static light scattering, and ¹H NMR. Light scattering analysis was performed using Astra 6.1 with a polymer dn/dc of 0.06. NMR analysis was performed using MestReNova version 14.2.1. Total polymer molecular weight was 31 kDa with PDI = 1.08, giving a calculated second block molecular weight of 12 kDa, and the second block composition was 61% BMA, 21% DMAEMA, and 18% PAA.

The polymer was then dissolved into 100% ethanol before dialysis in ultrapure water using a 6–8 kDa dialysis membrane. The resulting nanoparticles were frozen and lyophilized for storage. The lyophilized

polymer was resuspended using either ultrapure water or phosphate-buffered saline. The PBS-resuspended polymer was analyzed by dynamic light scattering (Malvern Zetasizer) for size and ζ potential. UV absorption at 210 nm, which corresponds to chain transfer agent adsorption, was measured in ultrapure water to determine the concentration using Beer's law.

Polymer-Peptide Conjugation. Lyophilized polymer was dissolved into DMF at 20 mg/mL and peptides were dissolved into DMF at 5 mg/mL. Two milliliter of polymer solution (2 mL) was mixed with 200 μ L of *N,N*-diisopropylcarbodiimide (1:1 molar ratio) and 150 µg of N-hydroxysuccinimide (2:1 molar ratio) with the polymer on ice for 20 min. 500 μ L of peptide solution was then added to the reaction mixture (1:1 polymer/peptide molar ratio) and brought to room temperature overnight. The peptide-polymer conjugates were then precipitated in 80/20% v/v pentane/diethyl ether and dried overnight before resuspension in either water or PBS. Peptide conjugation was analyzed using the fluorescent, aminereactive o-phthaldialdehyde (OPA) assay, and the yield was compared to peptide controls. Typical conjugation efficiency ranged between 50 and 70% of the feed ratio (Figure S3). Peptide-polymer conjugates were then resuspended in PBS before DLS analysis. Sample concentration was determined by using UV adsorption at 210 nm, referenced to unconjugated NP, to reduce variability from peptides and salts in the dried product.

Critical Micelle Concentration Determination. In a method derived by Wong et al., 69 the fluorescent dye 6-propionyl-2-(N,Ndimethylamino)naphthalene (PRODAN) is dissolved in methanol at a concentration of 10 μ M, 10 μ L of which is dispensed into each well of a black 96-well plate suitable for fluorescence assays (Greiner 655076) and allowed to dry completely. Serial dilutions of NP in PBS are made, ranging from 1 to 100 ng/mL. 200 µL portion of each dilution is added to each well in triplicate. The positive control is a 1% Triton-X solution, and the negative control is ultrapure water. The plate is incubated at 37 °C for 1 h before reading on a fluorescent plate reader (Biotek Cytation 5) with one excitation wavelength (325 nm) and two emission wavelengths: 435 nm, which corresponds with micelle-solubilized PRODAN and 532 nm, which corresponds with aqueous-phase PRODAN. At a critical micelle concentration, the ratio of 435-532 nm fluorescence increases suddenly, and from that point, increasing concentrations of NP yield higher relative 435 nm fluorescent emissions. CMC is reported as the concentration at which the 435-532 nm fluorescence ratio increases above the negative control's value.

NP siRNA Loading and Characterization. NP electrostatically loads siRNA due to the cationic polyDMAEMA block 1 of the polymer. As the pK_a of DMAEMA is 7.3, approximately 50% of DMAEMA is positively charged in PBS at pH 7.4. The molar ratio for 4:1 electrostatic NP/siRNA loading was found to be 2.93:1 NP/siRNA, which was confirmed through gel retardation assay as in Convertine and Benoit et al. Unless otherwise stated, all siRNA controls used Life Technologies Silencer Select Negative Control No. 2 siRNA (ThermoFisher 4390846).

Transmission Electron Microscopy. One μ g/mL NP solutions (1 μ g/mL) were prepared and submitted to the University of Rochester Medical Center's Electron Microscopy core for processing. Briefly, samples of approximately 1 μ g/mL in ultrapure water were dried on grids and stained with uranyl acetate. Grids were imaged by using a Hitachi 7650 transmission electron microscope.

Gene Knockdown Studies. Gene knockdown due to siRNA delivery was measured using the quantitative polymerase chain reaction (qPCR). Cells were treated with GAPDH siRNA (Thermo-Fisher 4404024)-loaded NPs at 4:1 polymer/siRNA charge ratio for 24 h in either serum-containing or serum-free (OptiMEM) media. The negative controls were cells treated with NP loaded with untargeted siRNA (ThermoFisher code 4390844). Cells then were lysed using TRK buffer, followed by repeated freeze-thaw cycles and plate scraping. The cell lysates were homogenized using homogenization columns (Omega HCR003) before RNA extraction (Omega RNACOL-02). Extracted RNA was treated with DNase on the columns before elution. RNA concentration was quantified using UV absorption, and cDNA synthesis was performed using 500 µg of RNA with a Bio-Rad iScript cDNA synthesis kit as per manufacturer's protocol. The resulting cDNA was then mixed with GAPDH and β -Actin primers separately at 20 μg scale with 500 nM primer concentrations (primer sequences listed in Table 3). Samples were

Table 3. Primer Sequences Used for PCR^a

gene		nucleotide sequence $(5' \rightarrow 3')$
GAPDH	forward	AGGTCGGTGTGAACGGATTTG
	reverse	TGTAGACCATGTAGTTGAGGTCA
β -actin	forward	ACTATTGGCAACGAGCGGTT
	reverse	CAGGATTCCATACCCAAGAAGGA

^aPrimers were acquired from Integrated DNA Technologies.

then run by using a Biorad CFX96 RT-PCR machine. Ct values of GAPDH were subtracted from β -actin for each sample to yield Δ Ct, which were then subtracted from the average of each plate's negative controls to yield $\Delta\Delta$ Ct for each condition.

Cellular Uptake. For cell siRNA uptake studies, AF488 labeled negative control siRNA (Qiagen AllStars Negative Control siRNA AF488, Catalog No. 1027292) was loaded at a 4:1 siRNA:corona electrostatic charge ratio. C3H10T1/2 cells acquired from ATCC were used as mesenchymal stem cells (MSCs) and treated at 30 nM siRNA for 24 h in either 1 g/L glucose Dulbecco's modified Eagle's medium supplemented with 10% fetal bovine serum (FBS) or, for serum-free conditions, OptiMEM with no supplementation. Labeled siRNA without an NP was used as a negative control. MSCs were then treated with trypsin, collected into tubes, and treated with 4% formaldehyde solution for fixation before washing with PBS. RAW 264.7 cells acquired from ATCC were used as a macrophage model and were treated with NP-loaded 10 nM siRNA for 2 h. Labeled siRNA without NP was used as a negative control. Cells were then scraped and collected into tubes before 4% formaldehyde fixation and PBS washing. Cells were analyzed by flow cytometry (BD Accuri C6+) and cells exhibiting 530 nm fluorescence greater than siRNA (no NP) controls were considered positive for NP. Mean fluorescence intensity at 530 nm was measured for all cells.

Alamar Blue Assay. Human umbilical vein endothelial cells (HUVECs) at 8000 cells/cm² were treated with 30 nM siRNA-loaded NPs at 4:1 NP/siRNA charge ratios for 24 h in endothelial growth media-2 (EGM-2; endothelial basal media-2 (EBM-2) containing EGM-2 SingleQuots) containing 10% FBS in 96-well cell culture plates. 10 μ L of Alamar Blue solution was added to each well 2 h before fluorescence intensity was measured on a BioTek Cytation 5 (545 nm ex/585 nm em). Values were normalized to untreated cells (Figure S3).

Heparin Displacement Assay. 4 μ M siRNA was loaded into NP at 4:1 charge ratio in PBS at pH 7.4 in 8 μ L total volume and incubated for 30 min before 1 μ L of human serum was added. Samples were incubated at 37 °C overnight before 1 μ L of sodium heparin (ThermoFisher A16198.06) was added to reach final heparin concentrations of 0.16, 0.32, 0.63, and 1.25 mg/mL at 10 μ L. Samples were incubated in heparin for 30 min at room temperature before being loaded into a 2% agarose gel cast in pH 7.4 TAE buffer. Free siRNA was loaded into the gel as a reference. Gels were run at 80 V for 30 min before being rinsed and stained in 1× SybrGold. The

fluorescence intensity of each siRNA band was compared to the free siRNA. Fluorescence intensity values were normalized to free siRNA controls, and the values were fit to a sigmoidal function with variable slope using GraphPad Prism's nonlinear fitting functions. The bottom values were fixed to 0 and the top values were fixed to 1 as the data were previously normalized. The outputs were a Hillslope coefficient (n) and EC₅₀ values corresponding to the point where 50% of siRNA was displaced. The resulting values were used in the following equation to calculate the heparin concentration (x) at which 90% of siRNA (y = 0.9) would be released

$$x = \left(\frac{(1-y) \times EC_{50}^{-n}}{y}\right)^{-1/n}$$
 (1)

90% release was chosen as an approximation of 100% release as this equation has a trivial solution for y = 0.5 and has no solution at y = 1. Error was propagated using 95% confidence intervals from the original fit values.

Hemolysis Assay. Human blood was retrieved from consenting donors by a trained phlebotomist in compliance with the University of Rochester's Institutional Review Board. Blood was collected in K2 ethylenediaminetetraacetic acid (EDTA) blood collection tubes. The blood was prepared and used for the hemolysis assay as described by Evans et al. 59 Briefly, the blood was separated at 500 RCF for 5 min, and the plasma was removed before an equal volume of pH 7.4 PBS. The erythrocytes were washed a total of three times by centrifugation and PBS. The washed erythrocytes were then suspended in a range of phosphate-buffered saline solutions at pH 7.4, 6.8, 6.2, and 5.6 at a 1:49 erythrocyte/PBS ratio. 20 µL of 15 µM siRNA-loaded NPs were then mixed with 180 μ L of erythrocytes at different pH values in quadruplicate in a clear 96-well plate. 1% Triton-X was used as a positive control, and pH-matched PBS was used for negative controls. Plates were incubated at 37 °C for 2 h and then centrifuged at 500 RCF for 5 min to separate intact cells from the supernatant. 100 μ L of supernatant from each sample was transferred to a clear 96-well plate. The absorbance of each sample was measured at 576 nm in a plate reader (BioTek Cytation 5). Negative controls were used to subtract background values from absorbance values and normalized to pHmatched positive controls.

Infrared Dye Labeling of the NP. NPs were labeled by exploiting the residual trithiocarbamate from the chain transfer agent used for synthesis in a one-pot aminolysis reaction adapted from Qiu et al. ⁷⁰ Briefly, 1 equiv NP suspended in ultrapure water was mixed with 100 mol equiv of *N,N*-diisopropylethylamine, and 1 equiv of maleimide-functionalized Cy7 (Biotium). After 2 h of reaction at room temperature, labeled NP was dialyzed against PBS for 24 h using 6–8 kDa dialysis tubing. NP solution was collected and total volume measured via mass to determine postdialysis concentration.

Pharmacokinetic Studies. All animal experiments were approved by the Institutional Animal Care and University Committee of Animal Resources (UCAR). Cy7-labeled NPs loaded with GFP siRNA (ThermoFisher AM4626) at a 4:1 charge ratio were administered to BALB/c mice under isofluorane anesthesia via retro-orbital injections (4 mg/kg, 100 μ L). Mice were placed on a heated platform, and their ears were fixed onto a flat riser under the lens. A ring illuminator fitted with a 730 \pm 20 nm band-pass filter was used for illumination. A Basler Ace monochrome acA1300-60 g camera fitted with a 800 nm long-pass filter was used for imaging and image capture. Fluorescence intensity of Cy7 was tracked before and for 30 min after injection via image capture at 0.5 Hz. For analysis, preinjection frames were subtracted from postinjection frames. Fluorescence intensity of the blood vessels was normalized to the maximum intensity observed. ROI were drawn in ImageJ around blood vessels near the base of the ear, and values were averaged together between ROI. The averaged intensity was then plotted against time and fit to a two-part exponential fit corresponding to a two-compartment pharmacokinetic model using GraphPad Prism 9.5.0, resulting in distribution phase and elimination phase half-lives. The concept for this technique was adapted from Nomoto et al.⁶⁵ and Jackson et al.30

Thermodynamic Calculations. The relationship between critical micelle concentration and Gibb's free energy is approximated by the equation ⁵⁰

$$\Delta G \approx RT \ln(\text{CMC})$$
 (2)

ASSOCIATED CONTENT

5 Supporting Information

The Supporting Information is available free of charge at https://pubs.acs.org/doi/10.1021/acsanm.4c01995.

Integrated ¹H NMR spectra of the diblock copolymer, MALDI-ToF analysis results for ZIPs, ZIP-NP conjugation yields, β -strand interaction modeling for ZIP–protein interactions, mesenchymal stem cell viability after NP dosing in the presence and absence of serum, human umbilical vein endothelial cell viability after NP treatment in serum, and macrophage uptake of NP in the presence and absence of serum (PDF)

AUTHOR INFORMATION

Corresponding Author

Danielle S. W. Benoit — Department of Biomedical
Engineering, University of Rochester, Rochester, New York
14627, United States; Center for Musculoskeletal Research,
University of Rochester, Rochester, New York 14642, United
States; Department of Chemical Engineering, University of
Rochester, Rochester, New York 14611, United States;
Materials Science Program, University of Rochester,
Rochester, New York 14627, United States; Department of
Bioengineering, Knight Campus for Accelerating Scientific
Impact, University of Oregon, Eugene, Oregon 97403, United
States; ② orcid.org/0000-0001-7137-8164;
Email: dbenoit@uoregon.edu

Authors

Clyde Overby — Department of Biomedical Engineering, University of Rochester, Rochester, New York 14627, United States; Center for Musculoskeletal Research, University of Rochester, Rochester, New York 14642, United States; orcid.org/0000-0001-7033-280X

Baixue Xiao — Department of Biomedical Engineering, University of Rochester, Rochester, New York 14627, United States; Center for Musculoskeletal Research, University of Rochester, Rochester, New York 14642, United States; orcid.org/0000-0001-8337-8401

Tiana Salomon — Department of Biomedical Engineering, University of Rochester, Rochester, New York 14627, United States; © orcid.org/0000-0002-7158-6235

Jorge Jimenez — Department of Biomedical Engineering, University of Rochester, Rochester, New York 14627, United States

Nathaniel Silvia — Department of Biomedical Engineering, University of Rochester, Rochester, New York 14627, United States

Complete contact information is available at: https://pubs.acs.org/10.1021/acsanm.4c01995

Notes

The authors declare no competing financial interest.

ACKNOWLEDGMENTS

Funding for this study was provided by the National Institutes of Health (NIH) (F31AR076874, R01DE018023, and R01AR056696) and the National Science Foundation (NSF) (CBET-1450897 and DMR-2103553). The authors thank Prof. James L. McGrath (University of Rochester, Biomedical Engineering) for using his laboratory equipment and Prof. Ron Wood (University of Rochester Medical Center, School of Medicine and Dentistry) for using his infrared imaging system. The content is solely the responsibility of the authors and does not necessarily represent the official view of the National Institutes of Health or National Science Foundation.

REFERENCES

- (1) Adams, D.; Gonzalez-Duarte, A.; O'Riordan, W. D.; Yang, C.-C.; Ueda, M.; Kristen, A. V.; Tournev, I.; Schmidt, H. H.; Coelho, T.; Berk, J. L.; et al. Patisiran, an RNAi therapeutic, for hereditary transthyretin amyloidosis. *N. Engl. J. Med.* **2018**, 379 (1), 11–21.
- (2) Creech, C. B.; Walker, S. C.; Samuels, R. J. SARS-CoV-2 vaccines. *JAMA* **2021**, 325 (13), 1318–1320.
- (3) Wang, L.; Zheng, W.; Liu, S.; Li, B.; Jiang, X. Delivery of CRISPR/Cas9 by novel strategies for gene therapy. *ChemBioChem* **2019**, 20 (5), 634–643.
- (4) Arany, S.; Benoit, D. S.; Dewhurst, S.; Ovitt, C. E. Nanoparticle-mediated gene silencing confers radioprotection to salivary glands in vivo. *Mol. Ther.* **2013**, *21* (6), 1182–1194.
- (5) Wang, Y.; Malcolm, D. W.; Benoit, D. S. W. Controlled and sustained delivery of siRNA/NPs from hydrogels expedites bone fracture healing. *Biomaterials* **2017**, *139*, 127–138.
- (6) Mitchell, M. J.; Billingsley, M. M.; Haley, R. M.; Wechsler, M. E.; Peppas, N. A.; Langer, R. Engineering precision nanoparticles for drug delivery. *Nat. Rev. Drug Discovery* **2021**, *20* (2), 101–124.
- (7) Anselmo, A. C.; Mitragotri, S. Nanoparticles in the clinic: An update. *Bioeng. Transl. Med.* **2019**, 4 (3), No. e10143, DOI: 10.1002/btm2.10143.
- (8) Sun, M.; Wang, K.; Oupicky, D. Advances in Stimulus-Responsive Polymeric Materials for Systemic Delivery of Nucleic Acids. *Adv. Healthcare Mater.* **2018**, 7 (4), No. 1701070.
- (9) Pelaz, B.; Alexiou, C.; Alvarez-Puebla, R. A.; Alves, F.; Andrews, A. M.; Ashraf, S.; Balogh, L. P.; Ballerini, L.; Bestetti, A.; Brendel, C.; et al. Diverse applications of nanomedicine. *ACS Nano* **2017**, *11* (3), 2313–2381.
- (10) Convertine, A. J.; Benoit, D. S.; Duvall, C. L.; Hoffman, A. S.; Stayton, P. S. Development of a novel endosomolytic diblock copolymer for siRNA delivery. *J. Controlled Release* **2009**, *133* (3), 221–229.
- (11) Benoit, D. S. W.; Henry, S. M.; Shubin, A. D.; Hoffman, A. S.; Stayton, P. S. pH-responsive polymeric sirna carriers sensitize multidrug resistant ovarian cancer cells to doxorubicin via knockdown of polo-like kinase 1. *Mol. Pharmaceutics* **2010**, *7* (2), 442–455.
- (12) Kopac, T. Protein corona, understanding the nanoparticle—protein interactions and future perspectives: A critical review. *Int. J. Biol. Macromol.* **2021**, *169*, 290–301.
- (13) Ke, P. C.; Lin, S.; Parak, W. J.; Davis, T. P.; Caruso, F. A Decade of the Protein Corona. ACS Nano 2017, 11 (12), 11773-11776
- (14) Malcolm, D. W.; Varghese, J. J.; Sorrells, J. E.; Ovitt, C. E.; Benoit, D. S. The Effects of Biological Fluids on Colloidal Stability and siRNA Delivery of a pH-Responsive Micellar Nanoparticle Delivery System. ACS Nano 2018, 12 (1), 187–197.
- (15) Barbero, F.; Russo, L.; Vitali, M.; Piella, J.; Salvo, I.; Borrajo, M. L.; Busquets-Fité, M.; Grandori, R.; Bastús, N. G.; Casals, E.; Puntes, V. Formation of the Protein Corona: The Interface between Nanoparticles and the Immune System. *Semin. Immunol.* **2017**, *34*, 52–60.

- (16) Parveen, R.; Shamsi, T. N.; Fatima, S. Nanoparticles-protein interaction: Role in protein aggregation and clinical implications. *Int. J. Biol. Macromol.* **2017**, *94* (Pt A), 386–395.
- (17) Hoffman, A. S. The early days of PEG and PEGylation (1970s-1990s). *Acta Biomater.* **2016**, *40*, 1–5.
- (18) Suk, J. S.; Xu, Q.; Kim, N.; Hanes, J.; Ensign, L. M. PEGylation as a strategy for improving nanoparticle-based drug and gene delivery. *Adv. Drug Delivery Rev.* **2016**, *99* (Pt A), 28–51.
- (19) Veronese, F. M.; Pasut, G. PEGylation, successful approach to drug delivery. *Drug Discovery Today* **2005**, *10* (21), 1451–1458, DOI: 10.1016/S1359-6446(05)03575-0.
- (20) Hatakeyama, H.; Akita, H.; Harashima, H. The polyethyleneglycol dilemma: advantage and disadvantage of PEGylation of liposomes for systemic genes and nucleic acids delivery to tumors. *Biol. Pharm. Bull.* **2013**, *36* (6), 892–899.
- (21) Papini, E.; Tavano, R.; Mancin, F. Opsonins and dysopsonins of nanoparticles: facts, concepts, and methodological guidelines. *Front. Immunol.* **2020**, *11*, No. 567365.
- (22) Papi, M.; Caputo, D.; Palmieri, V.; Coppola, R.; Palchetti, S.; Bugli, F.; Martini, C.; Digiacomo, L.; Pozzi, D.; Caracciolo, G. Clinically approved PEGylated nanoparticles are covered by a protein corona that boosts the uptake by cancer cells. *Nanoscale* **2017**, *9* (29), 10327–10334.
- (23) Zalba, S.; Ten Hagen, T. L.; Burgui, C.; Garrido, M. J. Stealth nanoparticles in oncology: Facing the PEG dilemma. *J. Controlled Release* **2022**, *351*, 22–36.
- (24) Miteva, M.; Kirkbride, K. C.; Kilchrist, K. V.; Werfel, T. A.; Li, H.; Nelson, C. E.; Gupta, M. K.; Giorgio, T. D.; Duvall, C. L. Tuning PEGylation of mixed micelles to overcome intracellular and systemic siRNA delivery barriers. *Biomaterials* **2015**, *38*, 97–107.
- (25) Joh, D. Y.; Zimmers, Z.; Avlani, M.; Heggestad, J. T.; Aydin, H. B.; Ganson, N.; Kumar, S.; Fontes, C. M.; Achar, R. K.; Hershfield, M. S.; Hucknall, A. M.; Chilkoti, A. Architectural Modification of Conformal PEG-Bottlebrush Coatings Minimizes Anti-PEG Antigenicity While Preserving Stealth Properties. *Adv. Healthcare Mater.* 2019, 8 (8), No. e1801177.
- (26) Walkey, C. D.; Olsen, J. B.; Guo, H.; Emili, A.; Chan, W. C. Nanoparticle size and surface chemistry determine serum protein adsorption and macrophage uptake. *J. Am. Chem. Soc.* **2012**, *134* (4), 2139–2147.
- (27) Tenzer, S.; Docter, D.; Kuharev, J.; Musyanovych, A.; Fetz, V.; Hecht, R.; Schlenk, F.; Fischer, D.; Kiouptsi, K.; Reinhardt, C.; Landfester, K.; Schild, H.; Maskos, M.; Knauer, S. K.; Stauber, R. H. Rapid formation of plasma protein corona critically affects nanoparticle pathophysiology. *Nat. Nanotechnol.* **2013**, *8* (10), 772–781.
- (28) Ishihara, T.; Takeda, M.; Sakamoto, H.; Kimoto, A.; Kobayashi, C.; Takasaki, N.; Yuki, K.; Tanaka, K.-i.; Takenaga, M.; Igarashi, R.; et al. Accelerated blood clearance phenomenon upon repeated injection of PEG-modified PLA-nanoparticles. *Pharm. Res.* **2009**, *26* (10), 2270–2279.
- (29) Ishida, T.; Kiwada, H. Accelerated blood clearance (ABC) phenomenon upon repeated injection of PEGylated liposomes. *Int. J. Pharm.* **2008**, 354 (1–2), 56–62.
- (30) Verhoef, J. J. F.; Anchordoquy, T. J. Questioning the Use of PEGylation for Drug Delivery. *Drug Delivery Transl. Res.* **2013**, 3 (6), 499–503.
- (31) Zhang, P.; Sun, F.; Liu, S.; Jiang, S. Anti-PEG antibodies in the clinic: Current issues and beyond PEGylation. *J. Controlled Release* **2016**, 244, 184–193.
- (32) Risma, K. A.; Edwards, K. M.; Hummell, D. S.; Little, F. F.; Norton, A. E.; Stallings, A.; Wood, R. A.; Milner, J. D. Potential mechanisms of anaphylaxis to COVID-19 mRNA vaccines. *J. Allergy Clin. Immunol.* **2021**, *147* (6), 2075.e2–2082.e2.
- (33) García, K. P.; Zarschler, K.; Barbaro, L.; Barreto, J. A.; O'Malley, W.; Spiccia, L.; Stephan, H.; Graham, B. Zwitterionic-coated "stealth" nanoparticles for biomedical applications: recent advances in countering biomolecular corona formation and uptake by the mononuclear phagocyte system. *Small* **2014**, *10* (13), 2516–2529.

- (34) Li, Y.; Liu, R.; Shi, Y.; Zhang, Z.; Zhang, X. Zwitterionic poly (carboxybetaine)-based cationic liposomes for effective delivery of small interfering RNA therapeutics without accelerated blood clearance phenomenon. *Theranostics* **2015**, *5* (6), 583.
- (35) Zhao, J.; Qin, Z.; Wu, J.; Li, L.; Jin, Q.; Ji, J. Zwitterionic stealth peptide-protected gold nanoparticles enable long circulation without the accelerated blood clearance phenomenon. *Biomater. Sci.* **2018**, *6* (1), 200–206.
- (36) Jackson, M. A.; Werfel, T. A.; Curvino, E. J.; Yu, F.; Kavanaugh, T. E.; Sarett, S. M.; Dockery, M. D.; Kilchrist, K. V.; Jackson, A. N.; Giorgio, T. D.; Duvall, C. L. Zwitterionic nanocarrier surface chemistry improves siRNA tumor delivery and silencing activity relative to polyethylene glycol. ACS Nano 2017, 11 (6), 5680–5696.
- (37) García, K. P.; Zarschler, K.; Barbaro, L.; Barreto, J. A.; O'Malley, W.; Spiccia, L.; Stephan, H.; Graham, B. J. S. Zwitterionic-coated "stealth" nanoparticles for biomedical applications: recent advances in countering biomolecular corona formation and uptake by the mononuclear phagocyte system. *Small* **2014**, *10* (13), 2516–2529, DOI: 10.1002/smll.201303540.
- (38) Yang, W.; Zhang, L.; Wang, S.; White, A. D.; Jiang, S. Functionalizable and ultra stable nanoparticles coated with zwitterionic poly (carboxybetaine) in undiluted blood serum. *Biomaterials* **2009**, *30* (29), 5617–5621.
- (39) Shao, Q.; Jiang, S. Molecular understanding and design of zwitterionic materials. *Adv. Mater.* **2015**, *27* (1), 15–26.
- (40) Dassonville, D.; Lécuyer, T.; Seguin, J.; Corvis, Y.; Liu, J.; Cai, G.; Mouton, J.; Scherman, D.; Mignet, N.; Richard, C. Zwitterionic Functionalization of Persistent Luminescence Nanoparticles: Physicochemical Characterizations and In Vivo Biodistribution in Mice. *Coatings* **2023**, *13* (11), No. 1913, DOI: 10.3390/coatings13111913.
- (41) Overby, C.; Park, S.; Summers, A.; Benoit, D. S. Zwitterionic peptides: Tunable next-generation stealth nanoparticle modifications. *Bioact. Mater.* **2023**, *27*, 113–124.
- (42) White, A. D.; Nowinski, A. K.; Huang, W.; Keefe, A. J.; Sun, F.; Jiang, S. Decoding nonspecific interactions from nature. *Chem. Sci.* **2012**, *3* (12), 3488–3494.
- (43) Katz, C.; Levy-Beladev, L.; Rotem-Bamberger, S.; Rito, T.; Rüdiger, S. G.; Friedler, A. Studying protein—protein interactions using peptide arrays. *Chem. Soc. Rev.* **2011**, *40* (5), 2131–2145.
- (44) Freeberg, M. A. T.; Farhat, Y. M.; Easa, A.; Kallenbach, J. G.; Malcolm, D. W.; Buckley, M. R.; Benoit, D. S.; Awad, H. A. Serpinel knockdown enhances mmp activity after flexor tendon injury in mice: Implications for adhesions therapy. *Sci. Rep.* **2018**, *8* (1), No. 5810.
- (45) Malcolm, D. W.; Freeberg, M. A. T.; Wang, Y.; Sims, K. R.; Awad, H. A.; Benoit, D. S. W. Diblock Copolymer Hydrophobicity Facilitates Efficient Gene Silencing and Cytocompatible Nanoparticle-Mediated siRNA Delivery to Musculoskeletal Cell Types. *Biomacromolecules* **2017**, *18* (11), 3753–3765.
- (46) Malcolm, D. W.; Sorrells, J. E.; Van Twisk, D.; Thakar, J.; Benoit, D. S. Evaluating side effects of nanoparticle-mediated siRNA delivery to mesenchymal stem cells using next generation sequencing and enrichment analysis. *Bioeng. Transl. Med.* 2016, 1 (2), 193–206.
- (47) Sims, K. R., Jr.; Maceren, J. P.; Liu, Y.; Rocha, G. R.; Koo, H.; Benoit, D. S. Dual antibacterial drug-loaded nanoparticles synergistically improve treatment of Streptococcus mutans biofilms. *Acta Biomater.* **2020**, *115*, 418–431.
- (48) Horev, B.; Klein, M. I.; Hwang, G.; Li, Y.; Kim, D.; Koo, H.; Benoit, D. S. pH-activated nanoparticles for controlled topical delivery of farnesol to disrupt oral biofilm virulence. *ACS Nano* **2015**, 9 (3), 2390–2404.
- (49) Wang, Y.; Newman, M. R.; Ackun-Farmmer, M.; Baranello, M. P.; Sheu, T.-J.; Puzas, J. E.; Benoit, D. S. Fracture-targeted delivery of β -catenin agonists via peptide-functionalized nanoparticles augments fracture healing. *ACS Nano* **2017**, *11* (9), 9445–9458.
- (50) Israelachvili, J. N.; Mitchell, D. J.; Ninham, B. W. Theory of self-assembly of hydrocarbon amphiphiles into micelles and bilayers. *J. Chem. Soc., Faraday Trans.* 2 **1976**, 72, 1525–1568.
- (51) Barenholz, Y. C. Doxil—The first FDA-approved nano-drug: Lessons learned. *J. Controlled Release* **2012**, *160* (2), 117–134.

- (52) Foldvari, M.; Chen, D. W.; Nafissi, N.; Calderon, D.; Narsineni, L.; Rafiee, A. Non-viral gene therapy: Gains and challenges of non-invasive administration methods. *J. Controlled Release* **2016**, 240, 165–190.
- (53) Kim, S. T.; Saha, K.; Kim, C.; Rotello, V. M. The Role of Surface Functionality in Determining Nanoparticle Cytotoxicity. *Acc. Chem. Res.* **2013**, 46 (3), 681–691.
- (54) Corbo, C.; Molinaro, R.; Parodi, A.; Toledano Furman, N. E.; Salvatore, F.; Tasciotti, E. The impact of nanoparticle protein corona on cytotoxicity, immunotoxicity and target drug delivery. *Nanomedicine* **2016**, *11* (1), 81–100.
- (55) Inglut, C. T.; Sorrin, A. J.; Kuruppu, T.; Vig, S.; Cicalo, J.; Ahmad, H.; Huang, H. C. Immunological and Toxicological Considerations for the Design of Liposomes. *Nanomaterials* **2020**, *10* (2), No. 190, DOI: 10.3390/nano10020190.
- (56) Nakamura, T.; Yamada, K.; Fujiwara, Y.; Sato, Y.; Harashima, H. Reducing the Cytotoxicity of Lipid Nanoparticles Associated with a Fusogenic Cationic Lipid in a Natural Killer Cell Line by Introducing a Polycation-Based siRNA Core. *Mol. Pharmaceutics* **2018**, *15* (6), 2142–2150.
- (57) Takano, S.; Aramaki, Y.; Tsuchiya, S. Physicochemical properties of liposomes affecting apoptosis induced by cationic liposomes in macrophages. *Pharm. Res.* **2003**, *20* (7), 962–968.
- (58) Merkel, O. M.; Beyerle, A.; Beckmann, B. M.; Zheng, M.; Hartmann, R. K.; Stöger, T.; Kissel, T. H. Polymer-related off-target effects in non-viral siRNA delivery. *Biomaterials* **2011**, 32 (9), 2388–2398.
- (59) Evans, B. C.; Nelson, C. E.; Shann, S. Y.; Beavers, K. R.; Kim, A. J.; Li, H.; Nelson, H. M.; Giorgio, T. D.; Duvall, C. L. Ex vivo red blood cell hemolysis assay for the evaluation of pH-responsive endosomolytic agents for cytosolic delivery of biomacromolecular drugs. *J. Visualized Exp.* **2013**, No. 73, No. e50166.
- (60) Gustafson, H. H.; Holt-Casper, D.; Grainger, D. W.; Ghandehari, H. Nanoparticle uptake: The phagocyte problem. *Nano Today* **2015**, *10* (4), 487–510.
- (61) Fam, S. Y.; Chee, C. F.; Yong, C. Y.; Ho, K. L.; Mariatulqabtiah, A. R.; Tan, W. S. Stealth coating of nanoparticles in drug-delivery systems. *Nanomaterials* **2020**, *10* (4), No. 787, DOI: 10.3390/nano10040787.
- (62) Schöttler, S.; Becker, G.; Winzen, S.; Steinbach, T.; Mohr, K.; Landfester, K.; Mailänder, V.; Wurm, F. R. Protein adsorption is required for stealth effect of poly (ethylene glycol)-and poly (phosphoester)-coated nanocarriers. *Nat. Nanotechnol.* **2016**, *11* (4), 372–377.
- (63) Bertrand, N.; Grenier, P.; Mahmoudi, M.; Lima, E. M.; Appel, E. A.; Dormont, F.; Lim, J.-M.; Karnik, R.; Langer, R.; Farokhzad, O. C. Mechanistic understanding of in vivo protein corona formation on polymeric nanoparticles and impact on pharmacokinetics. *Nat. Commun.* **2017**, 8 (1), No. 777.
- (64) Cai, R.; Chen, C. The crown and the scepter: roles of the protein corona in nanomedicine. *Adv. Mater.* **2019**, 31 (45), No. 1805740.
- (65) Nomoto, T.; Matsumoto, Y.; Miyata, K.; Oba, M.; Fukushima, S.; Nishiyama, N.; Yamasoba, T.; Kataoka, K. In situ quantitative monitoring of polyplexes and polyplex micelles in the blood circulation using intravital real-time confocal laser scanning microscopy. *J. Controlled Release* **2011**, *151* (2), 104–109.
- (66) Chang, L.; Perez, A. Ranking peptide binders by affinity with AlphaFold. *Angew. Chem.* **2023**, *135* (7), No. e202213362.
- (67) Trovato, A.; Chiti, F.; Maritan, A.; Seno, F. Insight into the structure of amyloid fibrils from the analysis of globular proteins. *PLoS Comput. Biol.* **2006**, 2 (12), No. e170.
- (68) Jiang, Y.; Li, P.; Zhao, J.; Liu, B.; Li, X. Iodonium Ylides as Carbene Precursors in Rh(III)-Catalyzed C-H Activation. *Org. Lett.* **2020**, 22 (19), 7475–7479.
- (69) Wong, J. E.; Duchscherer, T. M.; Pietraru, G.; Cramb, D. T. Novel Fluorescence Spectral Deconvolution Method for Determination of Critical Micelle Concentrations Using the Fluorescence Probe PRODAN. *Langmuir* 1999, 15 (19), 6181–6186.

(70) Qiu, X. P.; Winnik, F. M. Facile and Efficient One-Pot Transformation of RAFT Polymer End Groups via a Mild Aminolysis/Michael Addition Sequence. *Macromol. Rapid Commun.* **2006**, 27 (19), 1648–1653.